An Implantable Low-Power Ultrasonic Platform for the Internet of Medical Things

G. Enrico Santagati and Tommaso Melodia
Northeastern University, Boston, USA
{santagati, melodia}@ece.neu.edu

***Abstract*—Wirelessly networked systems of implantable medical devices endowed with sensors and actuators will be the basis of many innovative, sometimes revolutionary therapies. The biggest obstacle in realizing this vision of networked implantable devices is posed by the dielectric nature of the human body, which strongly attenuates radio-frequency (RF) electromagnetic waves. In this paper we present the first hardware and software architecture of an Internet of Medical Things (IoMT) platform with ultrasonic connectivity for intra-body communications that can be used as a basis for building future IoT-ready medical implantable and wearable devices. We show that ultrasonic waves can be efficiently generated and received with low-power and mm-sized components, and that despite the conversion loss introduced by ultrasonic transducers the gap in attenuation between $2.4\mathrm{GHz}$ RF and ultrasonic waves is still substantial, e.g., ultrasounds offer $70\mathrm{dB}$ less attenuation over $10\mathrm{cm}$. We show that the proposed IoMT platform requires much lower transmission power compared to $2.4\,\mathrm{GHz}$ RF with equal reliability in tissues, e.g., $35\,\mathrm{dBm}$ lower over $12\,\mathrm{cm}$ for 10^{-3} Bit Error Rate (BER) leading to lower energy per bit and longer device lifetime. Finally, we show experimentally that $2.4\mathrm{GHz}$ RF links are not functional at all above $12\,\mathrm{cm}$, while ultrasonic links achieve a reliability of 10^{-6} up to $20\,\mathrm{cm}$ with less than $0\,\mathrm{dBm}$ transmission power.**

I. Introduction

Wirelessly networked systems of implantable medical devices endowed with sensors and actuators will be the basis of many innovative and revolutionary therapies. *Artificial pancreases*, i.e., implanted continuous glucose monitors wirelessly interconnected with adaptive insulin pumps, could ease the life of many type-1 diabetic patients. *Post-surgery sensors* will detect changes in Ph or white cells concentration to prevent infections. Future *neurostimulators* will be composed of several miniaturized standalone stimulation devices that attach to different groups of neurons and wirelessly cooperate with each other to modulate the electrical signaling patterns and restore the functionalities of targeted organs. Future *pacemakers* will consists of sensing and pacing devices implanted in the heart chamber connected wirelessly with each other to enable advanced cardiac resynchronization therapy. Existing as well as futuristic applications of wireless technology to medical implants are growing into the new market of *"The Internet of Medical Things"* (IoMT).

Limitations of Current Wireless Technology. Unfortunately, the dielectric nature of the human body poses a key obstacle to enabling this vision of *networked implantable devices*. Biological tissues are composed primarily (65%) of water. Since radio-frequency (RF) waves are absorbed by aqueous tissues, higher transmission (Tx) power is needed to establish reliable links; this reduces the battery lifetime (or, equivalently, increases the battery size) of the implantable device, in a domain where low power, miniaturization, and battery duration are major concerns. To put this in context, state-of-the-art pacemakers require power in the order of $\mu\mathrm{W}$ for pacing [1], while commercial RF transceivers for implants operate in the order of tens of mW, making continuous telemetry operations prohibitive.

Ultrasonic Wireless Communications. Given the limitations of RF communications in human tissue, in this paper we present the design and implementation of an IoMT platform with ultrasonic wireless connectivity that can be used as a basis for building future medical implants that communicate safely, reliably and with low-power consumption through body tissues. Ultrasounds are mechanical waves that propagate at frequencies above the upper limit for human hearing, i.e., $20\mathrm{kHz}$. Compared to RF-waves, ultrasounds have significantly lower absorption in human tissues (e.g., around $70\,\mathrm{dB}$ less attenuation for a $1\mathrm{MHz}$ ultrasonic link compared to a $2.45\mathrm{GHz}$ RF link over $10-20\,\mathrm{cm}$ [2], [3], [4]). By using ultrasounds for connecting medical implants, patients will benefit from implants that provide wireless real-time telemetry while minimally affecting the battery lifetime of the device.

Prior Work. The idea of using ultrasonic waves for intra-body communications has been previously investigated in [5], [6], [7], [8]. In [5], the authors presented a channel model for ultrasonic intra-body communication, while in [6] the feasibility of nanoscale ultrasonic communications between nano-implants was studied. In [7], the authors investigated ultrasonic backscattering to enable communication between an external reader and an implantable device. In [8], [9], we proposed Ultrasonic WideBand (UsWB), an ultrasonic multipath-resilient physical (PHY) and medium access control (MAC) layer protocol, and experimentally demonstrated the feasibility of ultrasonic communications in tissue mimicking material. In [10], we presented an experimental Mbit/s ultrasonic transmission through ultrasonic phantoms, while in [11], [12] ultrasonic wireless transfer to power mm-sized implantable devices was demonstrated.

Paper Contribution. This paper presents the following core contributions:

- We present *the first hardware and software architecture of*

This material is based upon work supported by the National Science Foundation under grants CAREER CNS-1253309 and CNS-1618731.

an IoMT platform with ultrasonic connectivity for communications through body tissues. The IoMT platform consists of a modular and reconfigurable hardware and software architecture that can be flexibly adapted to different application and system requirements to enable telemetry, remote control of medical implants, as well and implant-to-implant communications.
- We discuss the implementation of two size-, energy-, and resource-constrained prototypes based on the IoMT platform architecture, i.e., an implantable IoMT-mote and a wearable IoMT-patch, that implement state-of-the-art ultrasonic communication protocols and communicate with each other through ultrasounds. *The IoMT-mote is the first miniaturized software-defined implantable device with ultrasonic communication and networking capabilities. We also demonstrate, for the first time, the feasibility of ultrasonic communications using miniaturized and energy constrained embedded devices.*
- We evaluate extensively the performance of the ultrasonic connectivity offered by the IoMT prototypes in terms of energy consumption and communication reliability using ultrasonic phantoms and porcine meat as communication media, and *for the first time compare this against state-of-the-art low-power RF-based wireless technologies* operating in the industrial, scientific, and medical (ISM) $2.4\mathrm{GHz}$ band, e.g., Bluetooth Low Energy (BLE). The ISM band is the RF band of choice for most current and future wireless medical devices, because it allows to interface medical devices with commercial devices such as smartphones, and offers larger bandwidth than other medical bands [13]. We show that ultrasonic waves can be efficiently generated and received with low-power and mm-sized components, and that despite the conversion loss introduced by ultrasonic transducers the gap between $2.4\mathrm{GHz}$ RF waves and ultrasonic attenuation is still substantial, e.g., ultrasounds offer $70\mathrm{dB}$ less attenuation over 10 cm. We show how the proposed IoMT platform requires much lower Tx power compared to BLE with equal reliability, e.g., $35\mathrm{dBm}$ lower Tx power over $12\mathrm{cm}$ for 10^{-3} Bit Error Rate (BER) leading to lower energy per bit cost and longer device lifetime. Finally, we show experimentally that BLE links are not functional at all above 12 cm, while ultrasonic links achieve 10^{-6} BER up to 20 cm with less than $0\,\mathrm{dBm}$ Tx power.

The remainder of the paper is organized as follows. In Section II, we describe the hardware and software architectures of the IoMT platform. In Section III and IV, we present the implementation of an IoMT-mote and an IoMT-patch. In Section V, we evaluate the performance of the IoMT ultrasonic connectivity, and we compare this with a state-of-the-art BLE chipsets. Finally, in Section VI, we conclude the paper.

II. IoMT Platform Architecture

The IoMT platform is a modular software and hardware architecture to be used as a basis for future low-power IoMT-ready wearable and implantable devices that communicate wirelessly through body tissues using ultrasounds. The IoMT

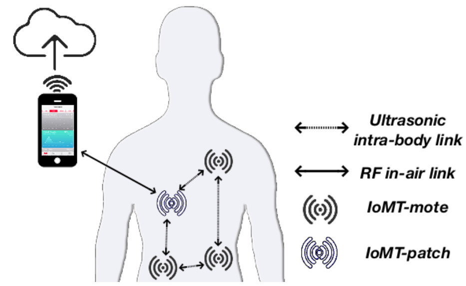

Fig. 1: IoMT-based System.

platform allows to (i) remotely measure, and store on the cloud physiological parameters of the patient measured by the implantable sensors (telemetry); (ii) remotely control actuators deployed in the body of the patient, e.g., stimulators, drug pumps, and pacing devices; (iii) enable closed-loop feedback applications through *implant-to-implant communications*, where actuators perform actions based on physiological data captured by sensors implanted elsewhere in the body. For example, a smart coronary stent could detect clogs and allow doctors to remotely monitor the patient condition and automatically trigger injection of drugs that prevent artery re-occlusion [14]. A smart neurostimulator can be triggered by a heart rate sensor to anticipate an epileptic attack [15].

Figure 1 shows an application scenario enabled by the IoMT platform. A set of sensors and actuators (IoMT-motes) are deployed inside the body of the patient and communicate with each other, or with wearable devices (IoMT-patches) through intra-body ultrasonic links (dotted lines). The IoMT-patches enable communication from the intra-body network to an access point connected to the Internet, e.g., a smartphone, through an RF link (continuous line).

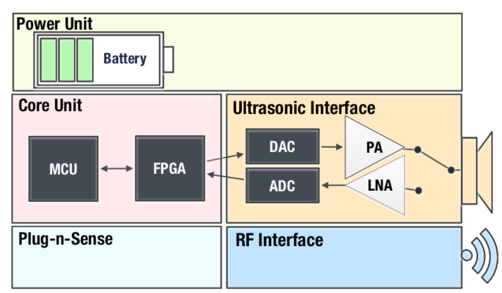

Fig. 2: IoMT platform hardware architecture.

A. Hardware Architecture

The IoMT-mote and the IoMT-patch are based on the ultrasonic IoMT platform modular hardware architecture shown in Figure 2. The *core unit* includes (i) a mm-size low-power field programmable gate array (FPGA) and (ii) a micro controller unit (MCU). Their combination offers hardware and software reconfigurability with very small packaging and low energy consumption. The miniaturized FPGA hosts the physical (PHY) layer communication functionalities. Reconfigurability at the physical layer is desirable - implants have often a lifetime of 5-10 years at least, while wireless standard chipsets have a lifetime of 1.5 years and become soon outdated. The MCU is in charge of data processing and of executing software-defined functionalities to implement flexible and reconfigurable upper-layer protocols, e.g., non-time critical MAC functionalities, network, transport and application. The *ultrasonic interface* enables ultrasonic wireless connectivity for both the IoMT-mote and the IoMT-patch, and consists of a receiver (Rx) and a transmitter (Tx) chain. The Rx chain includes a low-noise amplifier (LNA) and an analog-to-digital converter (ADC) to amplify and digital-convert received signals, while the Tx chain embeds a digital-to-analog converter (DAC) and a power amplifier (PA) to analog-convert and amplify the digital waveform before transmission. The hardware architecture also embeds an *RF interface* with an antenna to enable in-air RF wireless connectivity for example to connect the IoMT-patches to an access point. The *Plug-n-Sense (PnS) module* consists of a set of standard interfaces that allow the IoMT-mote to connect with different sensors, e.g., pressure and glucose sensors, to the ultrasonic IoMT platform according to the application and therapy requirements. The PnS module offers both standard digital and analog interfaces to accommodate different sensors. The *power unit* includes a battery and voltage regulation system for powering the device.

Figure 3 shows the mock-ups of the IoMT-mote and the IoMT-patch including the logic, the battery, the ultrasonic transducer, and the casing with desired target dimensions. Specifically, the IoMT-mote will be enclosed in a titanium biocompatible casing, while the IoMT-patch will be enclosed in a plastic casing and attached to a disposable adhesive patch.

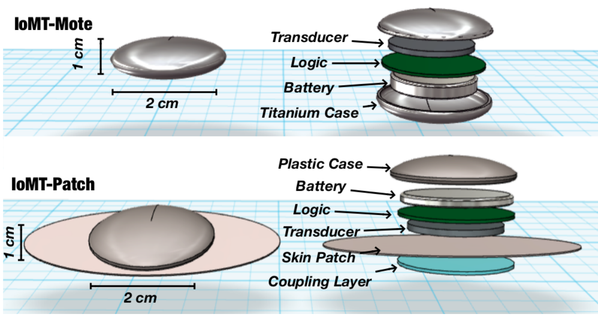

Fig. 3: Mock-ups of the IoMT-mote (top) and IoMT-patch (bottom)

B. Software Architecture

The IoMT platform includes a software-defined architecture designed to network IoMT-devices and encloses a set of PHY, data link and network layer functionalities that can flexibly adapt to the application and system requirements. The IoMT software framework also offers real-time reconfigurability at the application layer to develop application-specific data processing. In particular, sensor data processing applications running in the nodes are decomposed into *primitive building blocks* that can be arbitrarily arranged to create new sensing applications that fit the application requirements.

Figure 4 presents a high level description of the IoMT software architecture. The FPGA design implements the PHY layer communication functionalities, as well as the interfaces, e.g., SPI and I2C, to connect the FPGA chip with the MCU and the peripherals (DAC, ADC). The MCU software design

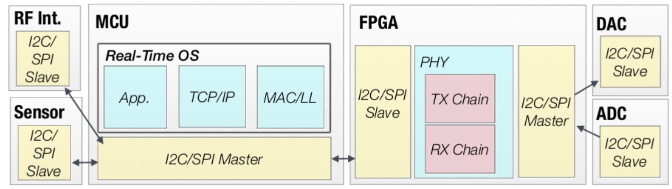

Fig. 4: IoMT platform software architecture.

is based on a real-time operating system (RTOS) and executes the upper layer communication functionality and protocol, e.g., link layer (LL), MAC, Network and Application layers. The MCU software design also defines SPI and I2C interfaces to enable data exchange between the MCU and the peripherals (FPGA, RF interface and sensors).

III. IoMT-Mote Prototype

We now present the design of the IoMT-mote prototype based on the the IoMT platform software and hardware architecture discussed in Section II. The IoMT-mote is the first miniaturized software-defined implantable device with ultrasonic communication and networking capabilities.

A. Hardware Implementation

Figure 5 shows the hardware implementation in the current alpha-prototype stage, i.e., using development boards for each component connected through wires. Red circles highlight the main integrated circuit in each development board. The ADC receives data directly from the Rx ultrasonic transducer. The FPGA outputs digital waveforms to the Tx ultrasonic transducers. The FPGA is connected to the MCU and ADC evaluation board through SPI interfaces as slave and master, respectively.

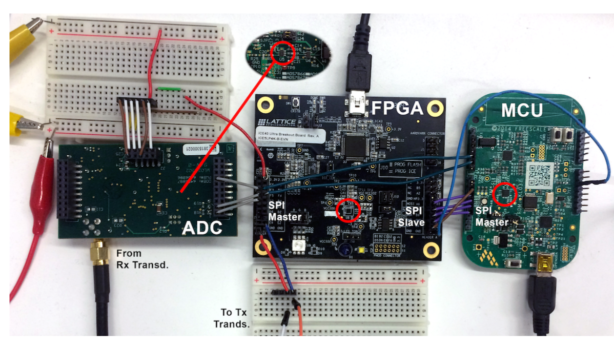

Fig. 5: Ultrasonic alpha-prototype node.

1) Core Unit: The *core unit* of the node includes (i) a *mm*-size low-power field programmable gate array (FPGA) and (ii) a micro controller unit (MCU).

FPGA. We use the Lattice Semiconductor iCE40 Ultra, which is currently the smallest, lowest power, and most integrated FPGA. It offers 4k look-up-tables (LUTs) in a very small package (2.08×2.08 mm) with very low static current drain (71 μA). We use the breakout evaluation board that provides the FPGA with a clock of 12 MHz.

MCU. The MCU is in charge of executing functionalities to coordinate the Tx/Rx operation and implement upper-layer protocols. We use the Freescale Kinetis KL03, a ultra-low-power ARM Cortex-M0+ MCU with an ultra-small package

$1.6 \times 2.0\mathrm{mm}$ specifically designed to develop smart and miniaturized devices. Tiny packaging and low-energy functionalities make KL03 the best existing match for our design. The KL03 also embeds a 12-bit ADC that can be used to interface the MCU with external analog sensors.

2) Ultrasonic Interface: The *ultrasonic interface* enables ultrasonic wireless connectivity through data converters, low-noise amplifiers (LNA), and custom ultrasonic transducers.

Ultrasonic Transducers. The IoMT-mote prototype embeds a custom-made and miniaturized *ultrasonic transducer* to generate and receive ultrasonic waves [16]. The custom transducer operates around $700\,\mathrm{kHz}$, and is based on a thin-disk piezoelectric element ($9.5\ \mathrm{mm}$ in diameter and $3\ \mathrm{mm}$ thick) with $200\,\mathrm{kHz}$ bandwidth. $700\,\mathrm{kHz}$ central frequency is good tradeoffs between attenuation of ultrasounds in tissue (increasing with frequency), thickness of the piezoelectric element (decreasing with frequency), available bandwidth (increasing with frequency), and radiation directivity (increasing with frequency) [2]. A diameter of $9.5\,\mathrm{mm}$ is a good compromise between size, conversion loss (increasing with smaller disks), and directionality (decreasing with smaller disks). For prototyping, the disk is embedded in an epoxy waterproof casing, which includes a coupling layer, electrodes, and a micro-coaxial cable. The final IoMT-mote will embed the raw piezoelectric disk, logic and battery in a titanium casing.

ADC. We based our current design on a small low-power ADC, i.e., TI ADS7883, sampling the received signal at $2\,\mathrm{MHz}$. The ADS7883 is connected to the FPGA through a SPI interface as slave peripheral and clocked by the FPGA that operates as SPI master. The SPI connection requires only three pins to output data through SPI protocol, i.e., clock, enable, and data out. This reduces the ADC size compared to parallel ADCs where samples are loaded in parallel requiring as many pins as the number of bits per sample.

Since the ADC operates serially on 12-bit samples with 4-bit padding, for a sampling rate of $2\mathrm{MHz}$ the SPI link operates at $32\,\mathrm{MHz}$, clocked by the SPI Master. To avoid unnecessary high dynamic power consumption, which is proportional to the circuit clock frequency, we use the ultra-low power PLL included in the iCE40 Ultra FPGA, to internally synthesize the $32\mathrm{MHz}$ clock from the $12\mathrm{MHz}$ clock on the FPGA evaluation board to individually drive the SPI Master block.

LNA. We implement a signal conditioning circuit using a low-noise, and low power operational amplifier (TI OPA835) in inverting configuration of gain 10 that shifts the signal to the desired DC offset required by the ADC input, i.e., $1.6\,\mathrm{V}$, and consumes as low as $250\mu\mathrm{A}$. To increase the receiver sensitivity and therefore be able to operate at lower Tx powers, we use a low-noise and variable gain amplifier (VGA), TI AD8338, before the signal conditioning circuit. The AD8338 offers low current consumption, i.e., $3\,\mathrm{mA}$, and a voltage controlled gain between $0-80\,\mathrm{dB}$. By reducing the Tx power we save energy at the transmitter, but we increase the power consumption at the receiver to power the preamplifier. Therefore, the use of the VGA can be very application dependent.

Tx Chain. In the Tx chain, we implemented a low-power, low-complexity and low-cost solution that does not require a DAC to convert digital waveforms to analog. In fact, because of the impulsive nature of the transmission scheme that we implement in this prototype (see Section III-B1), the system transmits digital square pulses from the digital output of the FPGA, with no need for analog conversion. The digital pulses are directly fed into the transducer that filters out the out-of-band frequency components, and therefore shapes *the square wave into a narrowband pulse centered at* $700\,\mathrm{kHz}$. Removing the DAC reduces the design size and energy consumption, as well as the complexity and cost of the device.

3) Power Unit: For the alpha-prototype stage the *power unit* consists of a commercial power supply that offers adjustable voltage level and facilitates prototyping. In the the final prototype, the power unit will accommodate a small implantable-grade battery with $3.3\ \mathrm{V}$ nominal voltage with a low-dropout (LDO) regulator.

B. Software Implementation

As discussed in Section II-B, the FPGA logic is mainly in charge of implementing the PHY layer functionality, while the MCU runs upper-layer protocols, as well as application layer functionality, such as sensor data acquisition and reconfigurable data processing operations. In the current prototype, we implemented the state-of-the-art UsWB transmission scheme and protocol [8]. UsWB is an impulse-based ultrasonic transmission and multiple access scheme based on short information-bearing carrierless ultrasonic pulses, following a pseudo-random adaptive time-hopping pattern with a superimposed adaptive spreading code.

1) FPGA Design: The FPGA top-level module instantiates Tx and Rx chain blocks implementing the UsWB transmitter and receiver, respectively, as well as the SPI, PLL and register manager modules.

UsWB PHY layer assumes time divided in slots of duration T_c, with slots organized in frames of duration $T_f = NT_c$, where N is the number of slots per frame. Each user transmits one pulse per frame in a slot determined by a pseudo-random time-hopping sequence. Bits are mapped into a pseudo-orthogonal code of variable length, M, and code chips are mapped into pulses through pulse position modulation (PPM). The pair code and frame length (M, N) can be adjusted to satisfy reliability constraints. Figure 6 shows a block diagram of the FPGA implementation. After several optimization cycles, the final implementation occupies around 99% of the available logic cells. As expected, the receiver logic occupies more than 50% of the available resources on the FPGA, most of which is dedicated to the synchronization process. To reduce the receiver complexity, the correlator templates used for synchronization are square-shaped waveforms of amplitude '-1' and '1', implemented using 2-bit coefficients.

Tx Chain Design. The Tx chain gets as input a stream of bytes coming from the MCU through the SPI Slave module, and outputs the PHY digital waveforms representing the modulated bits. Digital waveforms are then transmitted to the ultrasonic transducer that converts the electrical signal

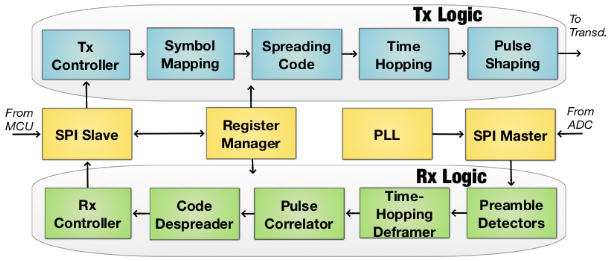

Fig. 6: Block scheme of the FPGA design.

to ultrasonic signal and radiates it in the communication channel. The Tx controller receives data from the MCU and coordinates the PHY layer operations of the Tx chain. In the Symbol Mapping block the information bits are mapped into {-1,1} binary symbols. The binary symbols are then spread in chips by the Spreading Code module. For each symbol, this block outputs M chips in {-1,1}. Chips are then forwarded to the Time-Hopping module that spreads them in time according to the selected time-hopping pattern, generated using a Linear Feedback Shifter Register (LFSR) module. Finally, the Pulse Shaping module maps the incoming chips to position-modulated pulses. The output is a train of position-modulated pulses following a predefined time-hopping pattern. Each pulse consists of three cycles of a $700\,\mathrm{kHz}$ square wave. A longer electrical excitation gives higher output pressure because of the resonant operation of the transducers. However, longer pulses lower the data rate. We found that three cycles provides a good compromise between data rate and ultrasonic generation efficiency. Finally, packets are preceded by two preambles: (i) a 64 cycles square wave that is used at the receiver for packet detection and (ii) a train of three pulses properly spaced in time used at the receiver for achieving time-hopping synchronization.

Rx Chain Design. The custom receiver chain implements the receiver UsWB PHY layer functionalities. The received ultrasonic signal is converted to an electrical signal by the Rx transducer. The signal is amplified by the LNA, and analog-to-digital converted by the ADC. Then, the custom receiver chain in the FPGA processes the digital waveform acquired through the SPI Master module. Finally, the receiver chain outputs a binary stream representing the received decoded data, which are delivered to the MCU through the SPI Slave module. The *Rx controller* triggers the start of the PHY layer processing when synchronization is achieved, and makes the decision on the received bits based on the output of the PHY layer processing blocks. The *preamble detectors* consist of a *packet* detector for coarse synchronization and a *time-hopping* synchronization block for fine synchronization. After synchronization is achieved, the *time-hopping deframer*, the *code despreader*, and *pulse correlator* invert the operation done at the transmitter, and the Rx controller makes a decision on the received bits.

Register Manager. The *register manager* is in charge of storing and routing in the design the configuration parameters written by the LL module running on the MCU on a pool of setting registers implemented on the FPGA. Through these setting registers, one can reconfigure key parameters of the PHY layer transmission scheme, and enable real-time reconfiguration of the transceiver. The communication system is designed to allow real-time reconfiguration of several parameters, e.g., spreading code and time-hopping frame length, among others.

SPI Module. The SPI interfaces enable communication with the external peripherals and the MCU. The *SPI Slave* block is driven by the SPI Master module of the MCU. This SPI link is used to exchange data between the MCU and the FPGA, such as data to be transmitted, received data or PHY configuration parameters. The data rate on this link is $1\,\mathrm{Mbit/s}$, which is greater than the PHY layer data rate, such that the PHY Tx chain is always backlogged. The *SPI Master block* drives the communication with the ADC. Specifically, the SPI Master triggers the sampling operations on the ADC, and reads back the sampled digital waveform.

PLL Module. The iCE40 Ultra includes an ultra-low power Phase Locked Loop (PLL) that provides a variety of user-synthesizable clock frequencies. We use the PLL to internally synthesize the $32\,\mathrm{MHz}$ clock signal to individually drive the SPI Master block as discussed in Section III-A2. The PLL module can be shut down when communication with the ADC is not needed to minimize the energy consumption.

2) Core MCU Firmware: The MCU software architecture is implemented on a RTOS to ease the development of complex software functionalities. We selected μTasker, which runs in resource constrained environments such as the KL03 MCU and offers support for the MCU low-power functionalities. Figure 7 shows the firmware architecture implemented on the KL03 MCU. In a typical application scenario, the application layer would trigger a reading through the PnS interface from a digital or analog sensor. The sensor reading is then processed by the reconfigurable data processing functionalities and passed to the LL protocol module for transmission through the SPI Master interface.

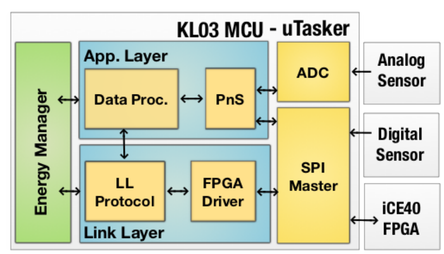

Fig. 7: KL03 MCU Firmware Architecture.

Link Layer. The UsWB LL protocol is in charge of managing the data transmission over the UsWB PHY layer interface. The connection is established through an advertising process initiated by a slave node, which transmits periodically advertising packets. A master node scans the advertising channel, and upon receiving an advertising packet, connects to the slave and both agree on a connection interval for exchanging data periodically. The connection uses a stop-and-wait flow control mechanism based on cumulative acknowledgements. The link layer also implements driver functionalities for the UsWB transceiver implemented on the FPGA that allow initializing the transceiver, configuring PHY layer parameters and triggering the transmitter and receiver operations.

Application Layer. The application layer implements the PnS module to connect the IoMT-mote with sensors. The PnS module consists of a digital I2C/SPI Master interface that connects to digital sensors, and an analog interface based on the MCU-embedded ADC that reads analog sensor outputs. Sensor data are processed by the reconfigurable and modular data processing module implemented on the MCU. Sensor data are encrypted end-to-end using a streamlined implementation of the Advanced Encryption Standard (AES) based on a 128bit key exchanged during paring between two devices.

The data processing module is based on the idea of decomposing the data processing applications running in the IoMT-mote into primitive blocks, and offering real-time reconfigurability at the application layer. The processing application consists of a sequence of basic operations that are executed on the sensed data to extract desired medical parameters. Based on this modular approach, applications can be represented by chains of binary sequences, i.e., keys. Each primitive function is mapped to a binary key. A concatenation of keys represents a concatenation of operations, and therefore represents an application. The IoMT-mote feeds these keys into an finite-state-machine (FSM) where each state represents a primitive block function. By parsing consecutive keys, the FSM transitions from state to state to process inputs and produce outputs.

Energy Manager. We leverage μTasker primitives to access the KL03 power states, and we implemented software functionalities to minimize the system energy consumption. Specifically, the energy management module is able to (i) adjust at runtime the core clock frequency according to the processing power required, (ii) select at runtime the low-power mode according to the application requirements, and (iii) implement automatic wake-up functionalities. The MCU current consumption can go from $1.8\,\mathrm{mA}$ in RUN state down to $0.6\,\mu$A in very-low-leakage-state, with other intermediate states that trade current consumption for wake-up time.

IV. IoMT-Patch Prototype

Here we describe the IoMT-patch implementation, focusing only on the modules that differ from the IoMT-mote.

A. MCU and RF Interface

The IoMT-patch prototype replaces the KL03 MCU with a TI CC2650 BLE wireless MCU that coordinates transmissions over the ultrasonic interface, as discussed in Section III-A1; and transmissions over the RF interface to connect the system with the access point. Specifically, we consider two different access point solutions: (i) a multi-platform smartphone app that communicates via BLE with the IoMT-patch and gives the user direct access to the sensed data, and (ii) a 6LOWPAN edge router that enables IPv6 connectivity and allows direct data delivery to the cloud. The TI CC2650 is the lowest-power and smallest $2.4\,\mathrm{GHz}$ wireless MCU currently available on the market, and is designed to operate in energy constrained systems powered by small coin cell batteries. The CC2650 device contains an ARM Cortex-M3 that implements upper layers of the BLE protocol stack and user defined functionalities. A secondary low-power ARM Cortex-M0 processor is in charge of lower-level BLE functionalities.

B. Software Implementation

We implemented two different firmwares for the TI CC2650 wireless MCU: (i) a BLE-enabled firmware based on TI-RTOS for connecting the IoMT patch to a smartphone, and (ii) an IPv6-enabled firmware based on Contiki that offers 6LOWPAN capabilities for IPv6 support [17]. Finally, we implemented a BLE-enabled access point through a smartphone app that delivers the sensed data to the user and a 6LOWPAN edge router that collects and publishes data on the cloud.

1) BLE-Enabled Implementation: The BLE-enabled firmware establishes the connection between the IoMT-patch and the BLE access point. The connection is established through an advertising process initiated by the IoMT-patch. When the access point receives an advertising packet, it sends a connection request to the slave and they start exchanging data every $2\,\mathrm{s}$. We considered the BLE Heart Rate Profile. In the background, the IoMT-patch initializes the ultrasonic intra-body link to retrieve the heart rate measurement from the IoMT-mote. Security in the over-the-air link is achieved through the frequency-hopping scheme adopted by the BLE physical layer, as well as end-to-end encryption. We developed an Android and iOS smartphone app based on the Qt framework, which implements a simple BLE heart listener that scans for BLE devices, connects to the Heart Rate service running on the IoMT-patch, and delivers the heart rate measurement to the user.

2) IPv6-Enabled Implementation: The IPv6-enabled firmware offers 6LoWPAN [17] encapsulation and header compression to support IPv6 over 802.15.4 wireless networks, and allows the IoMT-patch to connect to the Internet using open standards. The IoMT-patch is configured as a MQ Telemetry Transport (MQTT) client that periodically reads data from the IoMT-mote through the ultrasonic interface, and publishes sensor readings to a MQTT server. An edge router, i.e., a gateway between the 6LoWPAN mesh and Internet, provides conversion between 6LoWPAN and IPv6 header. We implement the edge router using the 6LBR 6LoWPAN Border Router solution [18] running on a Raspberry Pi.

V. Performance Evaluation

In this section we present the performance evaluation of the ultrasonic wireless interface implemented on the prototypes in terms of communication reliability and energy consumption. The ultrasonic wireless interface is responsible for enabling communications between the IoMT-patch and the IoMT-mote, and therefore its performance directly affects the lifetime of the implantable device, the most energy constrained device in the system. We also for the first time compare the ultrasonic wireless interface performance with the performance of an intra-body BLE link.

A. Hardware Current Consumption.

We measure the current consumption of the IoMT-mote prototype using a custom current sensing system based on the shunt resistor method. The shunt resistor method is based on of sensing a current by measuring the voltage drop along a small resistor connected in series between the power supply and the load. The current flowing through the resistor, thus the current drawn, is proportional to the measured voltage drop ($I = V/R$).

TABLE I: Current and power consumption of the IoMT-mote.

Component	Current [mA]		Power [mW]	
	Tx	Rx	Tx	Rx
MCU	1.8	1.8	6	6
FPGA	1.6	2.3	4	4.4
ADC	-	2	-	6.6
Preamp.	-	3	-	9
Tot.	3.4	9.1	10	26

In Table I, we report the current and power consumption of the IoMT-mote. We observe that the IoMT-mote consumes $9.1\ \mathrm{mA}$ in Rx mode, and as low as $3.4\ \mathrm{mA}$ in Tx mode. These results suggest that ultrasonic waves can be efficiently generated and received using low-energy and miniaturized components, which is a fundamental step towards proving the feasibility of miniaturizing the proposed IoMT platform. Moreover, we observe that the IoMT-mote can achieve power consumption comparable with commercial low-power wireless devices such as the TI CC2650 BLE MCU, which consumes $10.47\ \mathrm{mA}$ and $6.47\ \mathrm{mA}$ for Tx and Rx mode, respectively. Further optimization of the proposed hardware design could drastically reduce the power consumption and substantially outperform RF-based devices. For example, active power consumption during receiving and transmitting operations can be reduced by replacing the FPGA with an application-specific integrated circuit (ASIC). While it is hard to estimate the energy gain from replacing an FPGA with an ASIC, some studies suggest that the power reduction can be tenfold [19].

B. Propagation Loss.

Figure 8 shows the measured attenuation in porcine meat for RF waves at $2.4\,\mathrm{GHz}$ IMS and for ultrasounds at $700\,\mathrm{kHz}$. We also report simulated attenuation in tissue for $403.5\ \mathrm{MHz}$ MICS [4]. The attenuation includes absorption by tissue, conversion losses and spread losses. Measurements are performed by gradually increasing the amount of porcine meat between the transmitting and receiving antenna, or transducer. We confirm results reported in [2], [3] and observe that for $10\,\mathrm{cm}$ propagation distance, ultrasonic attenuation is $70\mathrm{dB}$ and $30\mathrm{dB}$ lower than RF $2.4\mathrm{GHz}$ IMS and $403.5\mathrm{MHz}$ MICS attenuation, respectively.

C. Bit Error Rate Evaluation

We now present the performance of the UsWB transmission scheme implementation on the IoMT-mote in terms of BER as a function of the Tx power in different scenarios. We vary the Tx power from $5\ \mathrm{dBm}$ ($3\ \mathrm{mW}$) to $-25\ \mathrm{dBm}$ ($3\ \mu\mathrm{W}$) by connecting attenuators between the FPGA output pin and the transducer. We used ultrasonic phantoms that match the acoustic properties of human tissues. Specifically, we used an upper arm phantom that emulates muscle tissue containing veins with fluid simulating blood, and a thoracic phantom that includes a thoracic spinal segment, muscle, and skin [20].

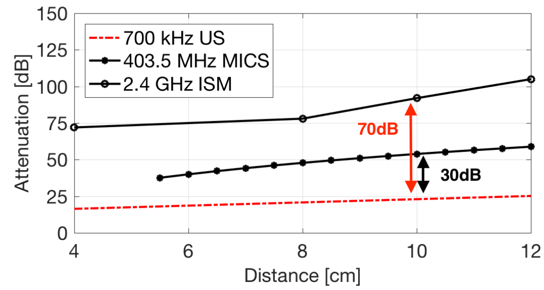

Fig. 8: Attenuation in porcine meat for RF $2.4\,\mathrm{GHz}$ IMS, RF $403.5\ \mathrm{MHz}$ MICS and for $700\ \mathrm{kHz}$ ultrasounds as a function of propagation distance.

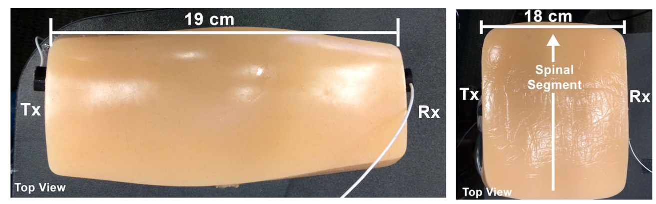

Fig. 9: Experiment setup for the upper arm phantom (left) and thoracic phantom (right).

Upper Arm Phantom. We place the two transducers facing each other on opposite sides of the upper arm phantom along $19\,\mathrm{cm}$, as shown in Fig. 9 (left). Figure 10 shows the BER as a function of the Tx power, for code length varying in $\{1, 5\}$ and frame length 1 (center) and 2 (top), when no preamplifier is used. We observe that the spreading code scheme mitigates the signal distortion, thus reducing channel errors.

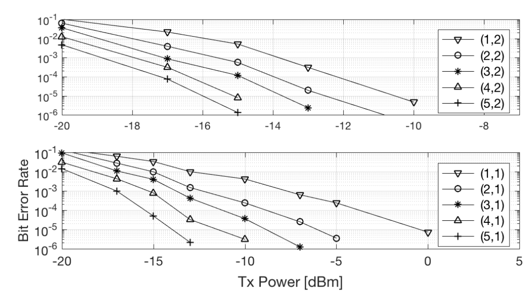

Fig. 10: BER for the no-amp scenario in the upper arm phantom for code length in $\{1, 5\}$ and frame length 2 (top) and 1 (bottom).

In this setup, the prototype achieves $90\ \mathrm{kbit/s}$, with code length 1 and frame length 2, i.e., pair (1,2) with a 10^{-6} BER with an input power at the Tx transducer of about $-10\,\mathrm{dBm}$ ($0.1\,\mathrm{mW}$). A data rate up to about $180\,\mathrm{kbit/s}$ can be achieved (also with 10^{-6} BER) with pair (1,1) increasing the input power to $0\,\mathrm{dBm}$ ($1\,\mathrm{mW}$). Lower-power transmissions are also possible by compensating with longer spreading code. For example, in the current implementation, for a Tx power of $-15\ \mathrm{dBm}$ ($30\ \mu\mathrm{W}$), and with a code length of 5 and frame length of 2, we obtain a data rate of $18\ \mathrm{kbit/s}$ with a BER lower than 10^{-6}.

Thoracic Phantom. We place the two transducers facing each other, $18\,\mathrm{cm}$ apart, as shown in Fig. 9 (right). The thoracic phantom allows to test the communication performance through heterogeneous soft/hard tissues.

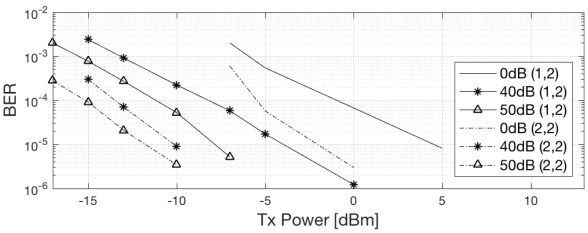

Fig. 11: BER in the thoracic phantom for code length in$\{1, 2\}$, frame length 2 and different amplification gains.

Figure 11 shows BER as a function of Tx power for frame 2, code length 1 and 2, for different value of amplification gain at the receiver, compared to the 0-gain scenario when no preamplifier is used. Because of the higher path loss and multipath effect caused by the soft-hard tissue interface, we observe an increase of $15\,\mathrm{dBm}$ in Tx power to achieve the same BER performance of the upper arm scenario when no preamplifier is used. By introducing a gain at the receiver, we increase the receiver sensitivity and therefore we are able to operate at lower Tx powers. By using $40\,\mathrm{dB}$ gain and $50\,\mathrm{dB}$ gain, we can get $90\,\mathrm{kbit/s}$ with 10^{-6} BER with $0\,\mathrm{dBm}$ and $-8\,\mathrm{dBm}$ Tx power, respectively. Because of the impedance mismatch between the transducer and the preamplifier, the Tx power does not decrease linearly with the receiver gain. Therefore, in the future prototype an impedance matching circuit will be required to compensate for this loss. Whether or not to use the preamplifier depends on the application scenario considered, and it should account for other design requirements, such as size and design complexity.

D. RF $2.4\,\mathrm{GHz}$ Vs. Ultrasounds

Packet Error Rate (PER). Here we compare UsWB transmission scheme implemented in the IoMT-mote with the BLE PHY layer based on a $1\,\mathrm{Mbit/s}$ Gaussian frequency shift key (GFSK) implemented on the TI CC2650 in terms of PER through porcine meat. Porcine meat closely emulates human muscular tissues [21], [22], and allows to evaluate side by side ultrasonic and RF communications in terms of reliability and energy consumption. For the IoMT-mote, we consider a setup where ultrasonic transducers are facing each other $12\,\mathrm{cm}$ apart, as shown in Figure 12. The PER is obtained as the ratio between the number of packets received with errors, and the total number of packets transmitted. Figure 13 (top) shows the IoMT-mote PER as a function of the Tx power, for code and frame length in $\{1,\,2\}$. For 10^{-6} BER, the prototype achieves $180\,\mathrm{kbit/s}$, with code and frame length 1, with a Tx power of about $-20\,\mathrm{dBm}$ ($10\,\mu\mathrm{W}$). By using frame length 2 to get rid of the ISI effect, we achieve $90\,\mathrm{kbit/s}$ data rate, with the same 10^{-6} BER, and Tx power of $-27\,\mathrm{dBm}$ ($2\,\mu\mathrm{W}$). Figure 13 (center) shows the PER performance of BLE in porcine meat as a function of the Tx

Fig. 12: Experiment setup for porcine meat scenario along $12\,\mathrm{cm}$.

power for different communication distances. We observe that for distances longer than $10\,\mathrm{cm}$, reliability drops dramatically. Specifically, for $12\,\mathrm{cm}$ distance, the PER becomes as high as 80% with the maximum Tx power available, i.e., $5\,\mathrm{dBm}$, making communication almost unfeasible. With higher distances, the communication is completely disrupted. In Fig. 13 (bottom), we compare PER performance of BLE over a $12\,\mathrm{cm}$ distance with the IoMT-mote performance (code and frame length 1). We observe that BLE requires around $35\mathrm{dBm}$ higher Tx power to achieve the same reliability as the IoMT-mote. This gap can be further increased by implementing stronger synchronization and decoding operations at the PHY layer.

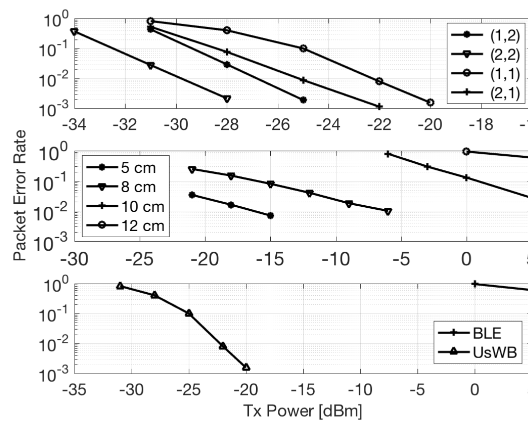

Fig. 13: IoMT-mote PER in porcine meat for code and frame length in $\{1,2\}$ (top). BLE PER in porcine meat for different communication distances (center). BLE and IoMT-mote PER in $12\,\mathrm{cm}$ porcine meat (bottom).

Energy per Bit and Device Lifetime. We consider a remote monitoring application in which 20 bytes of data are sent every minute between two devices. We compare the energy consumption of the IoMT-mote with the energy consumption of the CC2650 BLE devices, assuming current consumption values reported in Section V-A. We define energy per bit, E_b, as the ratio between the total energy spent by the two devices for exchanging information data over the amount of successfully exchanged information data [J/bit]. Network lifetime is the minimum between the Tx and Rx device's battery lifetime [years]. For the BLE devices, the master node connects, and the connection stays open with a connection event happening every $32\,\mathrm{s}$, i.e., the maximum connection interval available. In this scenario, we measure E_b equal to $0.77\,\mu\mathrm{J/bit}$ for BLE against $0.37\,\mu\mathrm{J/bit}$ for the IoMT-mote. We consider transmitting, receiving, processing and idle states only. Processing state occurs before and after a packet transmission and reception, and we assume a consumption of

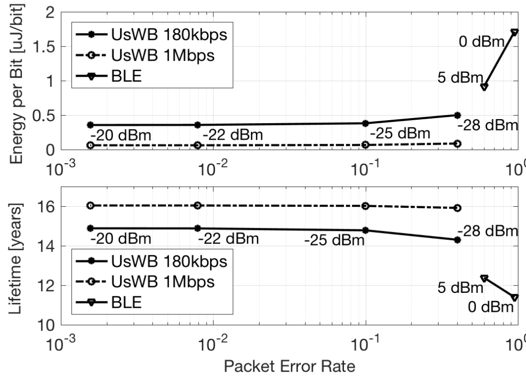

Fig. 14: IoMT-mote and BLE E_b (top) and lifetime (bottom) in porcine meat.

$3\,\mathrm{mA}$. We also assume $2\,\mu\mathrm{A}$ idle current consumption, and a $300\,\mathrm{mAh}$ battery. Under these conditions, the BLE network lifetime is 12.5, against 14.8 years achieved by the IoMT-mote.

In Fig. 14, we show the E_b (top) and the network lifetime (bottom) using the PER measurements discussed above. We observe that over $12\,\mathrm{cm}$ the IoMT-mote outperforms BLE in terms of lifetime and E_b. In fact, the IoMT-mote can achieve much lower PER with lower Tx power, and therefore keep the E_b and network lifetime close to the ideal values of 14.8 years achieved when PER is ideally zero. On the other hand, BLE can only operate over $12\,\mathrm{cm}$ at the maximum Tx power, still underperforming in terms of PER compared to the IoMT-mote. This further reduces the network lifetime and increases the E_b. Specifically, the IoMT-mote allows almost two more years of operations while achieving much higher reliability than BLE, i.e., about three order of magnitude lower PER. In Fig. 14 we also show how the the IoMT-mote E_b and lifetime performance would scale if we increased the data rate from $180\mathrm{kbit/s}$ to $1\mathrm{Mbit/s}$ to match the BLE data rate. This can be achieved using wider-bandwidth ultrasonic transducers and/or using higher order modulation schemes. Results show how E_b can become as low as $0.07\,\mu\mathrm{J/bit}$ and network lifetime increase up to 16 years.

VI. Conclusions

We presented the first hardware and software architecture of an IoMT platform with ultrasonic connectivity for intra-body communications, and for the first time we compared ultrasonic intra-body connectivity against state-fo-the-art low-power RF-based wireless technology. We showed that ultrasonic waves can be efficiently generated and received with low-power and mm-sized components, and that ultrasonic communications require much lower Tx power compared to BLE with equal reliability leading to lower energy per bit cost and longer device lifetime. We also show experimentally that BLE links are not functional at all above $12\,\mathrm{cm}$, while ultrasonic links achieve a reliability of 10^{-6} up to $20\,\mathrm{cm}$ with less than $0\mathrm{dBm}$ Tx power. By using wider-band transducers and further optimizing the hardware consumption of the prototypes E_b can become one order of magnitude lower than BLE, and achieve even longer device lifetime.

VII. Acknowledgement

The authors would like to thank Giulia Alberto for helping in the development of the IoMT-patch prototype.

References

[1] A. Al-Ahmad, K. Ellenbogen, A. Natale, and P. Wang, *Pacemakers and Implantable Cardioverter Defibrillators: An Expert's Manual:*. Cardiotext Publishing, 2010.

[2] L. Galluccio, T. Melodia, S. Palazzo, and G. E. Santagati, "Challenges and Implications of Using Ultrasonic Communications in Intra-body Area Networks," in *Proc. of IEEE Intl. Conf. on Wireless On-demand Networked Systems (WONS)*, Courmayeur, Italy, Jan. 2012.

[3] D. Kurup, W. Joseph, G. Vermeeren, and L. Martens, "Path loss model for in-body communication in homogeneous human muscle tissue," *Electronics Letters*, vol. 45, no. 9, pp. 453–454, 2009.

[4] K. Sayrafian-Pour, W.-B. Yang, J. Hagedorn, J. Terrill, and K. Yazdandoost, "A statistical path loss model for medical implant communication channels," in *Personal, Indoor and Mobile Radio Communications, 2009 IEEE 20th International Symposium on*, 2009, pp. 2995–2999.

[5] Y. Davilis, A. Kalis, and A. Ifantis, "On the use of ultrasonic waves as a communications medium in biosensor networks," *IEEE Transactions on Information Technology in Biomedicine*, vol. 14, no. 3, May 2010.

[6] T. Hogg and R. A. Freitas, "Acoustic Communication for Medical Nanorobots," *Nano Communication Networks (Elsevier)*, vol. 3, no. 2, pp. 83–102, Feb 2012.

[7] M. Peisino and P. Ryser, *Deeply Implanted Medical Device Based on a Novel Ultrasonic Telemetry Technology*. EPFL, 2013.

[8] G. Santagati, T. Melodia, L. Galluccio, and S. Palazzo, "Medium access control and rate adaptation for ultrasonic intra-body sensor networks," *IEEE/ACM Transactions on Networking*, vol. 24, pp. 1121–1134, Aug. 2015.

[9] G. Santagati and T. Melodia, "Experimental evaluation of impulsive ultrasonic intra-body communications for implantable biomedical devices," *IEEE Transactions on Mobile Computing*, vol. 16, no. 2, pp. 367–380, 2016.

[10] E. Demirors, G. Alba, G. E. Santagati, and T. Melodia, "High data rate ultrasonic communications for wireless intra-body networks," in *Proc. of IEEE Symposium on Local and Metropolitan Area Networks (LANMAN)*, Rome, Italy, June 2016.

[11] R. Guida, G. E. Santagati, and T. Melodia, "A 700 khz ultrasonic link for wireless powering of implantable medical devices," in *2016 IEEE SENSORS*, Oct 2016.

[12] J. Charthad, M. J. Weber, T. C. Chang, M. Saadat, and A. Arbabian, "A mm-sized implantable device with ultrasonic energy transfer and rf data uplink for high-power applications," in *Proceedings of the IEEE 2014 Custom Integrated Circuits Conference*, Sept 2014, pp. 1–4.

[13] Medical Device Radiocommunications Service (MedRadio), https://goo.gl/pjKY4C.

[14] D. S. et Al., "Bioresorbable electronic stent integrated with therapeutic nanoparticles for endovascular diseases," *ACS Nano*, vol. 9, no. 6, pp. 5937–5946, 2015.

[15] F. Sun and M. Morrell, "Closed-loop neurostimulation: The clinical experience," *Neurotherapeutics*, vol. 11, no. 3, pp. 553–563, 2014.

[16] APC International Ltd., "First Steps towards Piezoaction," https://www.americanpiezo.com.

[17] N. Kushalnagar, I. Corp, J. Hui, D. Culler, and A. R. Corp, "Transmission of ipv6 packets over ieee 802.15.4 networks," in *RFC 4944*, 2007.

[18] L. Deru, S. Dawans, M. Ocaña, B. Quoitin, and O. Bonaventure, *Redundant Border Routers for Mission-Critical 6LoWPAN Networks*. Cham: Springer International Publishing, 2014, pp. 195–203.

[19] I. Kuon and J. Rose, "Measuring the gap between fpgas and asics," in *Proceedings of the 2006 ACM/SIGDA 14th International Symposium on Field Programmable Gate Arrays*, ser. FPGA '06, 2006, pp. 21–30.

[20] "Blue Phantom Ultrasound Training Models," http://www.bluephantom.com/.

[21] C. R. Mol and P. A. Breddels, "Ultrasound velocity in muscle," *The Journal of the Acoustical Society of America*, vol. 71, no. 2, pp. 455–461, 1982.

[22] T. Koch, S. Lakshmanan, S. Brand, M. Wicke, K. Raum, and D. Morlein, "Ultrasound velocity and attenuation of porcine soft tissues with respect to structure and composition: I. muscle," *Meat Science*, vol. 88, no. 1, pp. 51 – 58, 2011.